

See discussions, stats, and author profiles for this publication at: <http://www.researchgate.net/publication/275719397>

# Nano-nickel catalyst reinforced with silicate for methane decomposition to produce hydrogen and nanocarbon: synthesis by co-precipitation cum modified Stöber method

ARTICLE *in* RSC ADVANCES · MAY 2015

Impact Factor: 3.71 · DOI: 10.1039/C5RA07098H

---

DOWNLOADS

5

---

VIEWS

13

## 2 AUTHORS, INCLUDING:



Upm Ashik

University of Malaya

6 PUBLICATIONS 32 CITATIONS

[SEE PROFILE](#)



Cite this: RSC Adv, 2015, 5, 46735

# Nano-nickel catalyst reinforced with silicate for methane decomposition to produce hydrogen and nanocarbon: synthesis by co-precipitation cum modified Stöber method

U.P.M. Ashik, W.M.A. Wan Daud\*

Received 20th April 2015  
Accepted 1st May 2015

DOI: 10.1039/C5RA07098H  
[www.rsc.org/](http://www.rsc.org/)

Co-precipitation cum modified Stöber method is a continuous process avoiding application of higher temperature treatment before supporting nano-metal with SiO<sub>2</sub>, irrespective of pre-experimented methods. We have resumed co-precipitation process without undertaking calcination under air in order to avoid even a partial particle agglomeration and hence maintained average particle size ~30nm after enforcing with SiO<sub>2</sub>. It is a first report adopting such an unceasing preparation for preparing metal/silicate nano-structures. Furthermore, Ni/SiO<sub>2</sub> nano-structured catalyst used for thermocatalytic decomposition of methane to produce hydrogen and carbon nanotubes. Experimented catalyst found very stable and the methane transformation activity endured 300 minutes on methane stream without going much deactivation at temperature range 475°C-600°C and did not completely deactivated, irrespective of many reported catalysts designating the resistance capability of analyzed nano-structured catalyst. We have successfully extended catalyst preparation method for Fe and Co metals and conducted preliminary catalyst examinations.

## Introduction

Nano-structured materials recently attracted intensively by research scholars mainly because of its inbuilt characteristics. Biology, optics, electronics, magnetism, sensing, etc. are some fields, chiefly working with nano-structures. While, nano-structures produced by applying Stöber method is hardly in catalysis nowadays<sup>1-8</sup>. Recent studies reveals that the enforcement of nano-materials with inert protective support can enhance compatibility of the nano-material which leads to change electron charge, reactivity and functionality of the material<sup>9-11</sup>. Furthermore, nano-metal/support composites unveil entirely dissimilar and advanced properties from those of individual metal and support materials<sup>12</sup>. Nano-Ni particles have large specific surface area and obviously have large number of active sites leads to have intrinsic surface

effects. While, those nanoparticles tend to aggregate at high temperature and hence results in low catalytic stability at higher temperature. However, shielding of nanoparticle with porous, stable and inert silicates prevent particle agglomeration and gear up catalyst for higher temperature performance. Silicate supported materials have a merit of exhibiting a synergetic effect of both metal and support materials. However, in the case of n-Ni/SiO<sub>2</sub> materials, active Ni phase provide the activity and the porous silica support makes room for a reaction similar to mesoporous silica.

To the best of authors' knowledge, it is first time applying n-Ni/SiO<sub>2</sub> catalyst prepared with co-precipitation cum modified Stöber method for thermocatalytic decomposition of methane (TCD) for the co-production of hydrogen and nano carbon. Establishment of clean hydrogen fuel, which does not produce any greenhouse gases (GHG) while its

combustion, can profoundly eliminate two major contemporary era challenges like energy crisis and environmental pollution from GHGs emitting from fuel combustion. The major resources and preparation methods for hydrogen are schematized in Fig. 1. Cell technology, petroleum refining, food, electronics, metallurgical processing industries and many other fields can be fueled by hydrogen and hence attracted tremendous attention by current researchers<sup>13-16</sup>. Global statistics demonstrate that 48% of hydrogen is producing form natural gas, which is equal to 240 Billion cubic meters (Bcm)/year. While, 30% (150Bcm/year) from petroleum, and 18% (90Bcm/year) from coal. Regrettably, only 4% (20Bcm/year) is obtained through water electrolysis without producing any GHG<sup>17, 18</sup>. There are different types of methods were developed for hydrogen production, such as bio-hydrogen production, reviewed elsewhere<sup>19</sup>, steam reforming of methane (SRM), partial oxidation (POX), coal gasification, water splitting, biomass gasification and thermochemical processes<sup>20-23</sup>. Water splitting process is really enthusiastic as it consumes only renewable solar and wind energy, but not economical because of its very low efficiency and higher processing cost. Furthermore, gasification and reforming of biomass are extensively explored for producing hydrogen from several biomass resources such as forest residues, wood wastes, crop residues, waste water treatment, biogas, etc.<sup>24, 25</sup>. While, requirement of supplementary separation/purification treatments are the major limitations of these technologies which reduces hydrogen selectivity<sup>26</sup>. SRM and POX are the normally accepting methods for producing hydrogen from methane gas. Among them, SRM has been considered as the most commonly adopted technique for recent years. Although, SRM needs higher process energy and results in the production of enormous CO<sub>x</sub> (at least 1mol of CO<sub>2</sub>/mol of converted methane) irrespective of its comparatively higher process efficiency (50%)<sup>13</sup>. Likewise, the POX process is also causes massive GHG emission. Subsequently, thermocatalytic decomposition of methane (TCD) attracted as a novel technique for eco-friendly hydrogen production. In this moderately endothermic process, methane is thermally decomposed to solid carbon and gaseous

hydrogen in a technically simple one step process as shown in equation (1).



Moreover, TCD process can enhance the production rate of single and multi-walled carbon nanotubes and fibers with high mechanical strength, irrespective of the arc-discharge evaporation to produce single wall carbon nanotubes<sup>27</sup>.

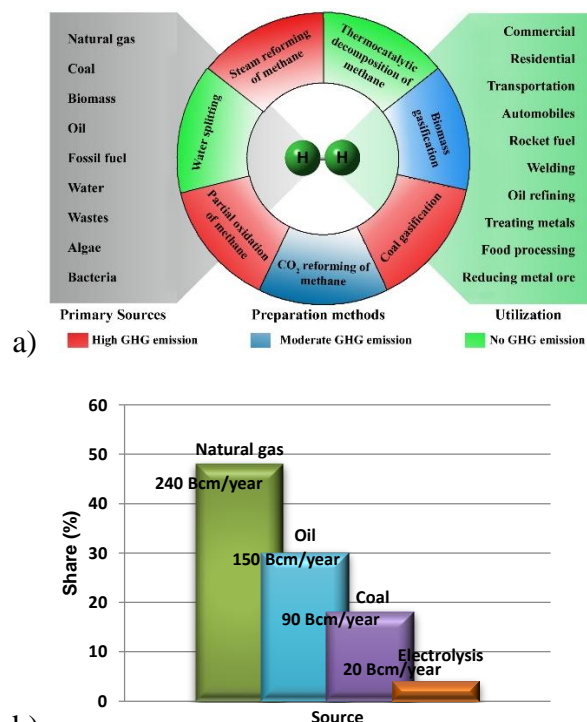


**Fig. 1** a) Schematic representation of the sources, preparation methods and utilization of hydrogen and b) worldwide hydrogen production by sources (Reprinted with permission from Elsevier Limited)<sup>17</sup>

In general, catalytic deactivation during TCD process is mainly because of the huge carbon deposition over the catalyst with time. This faster deactivation is the major challenge in TCD and studies are continuously performing to develop a catalysts with longer life as well as higher activity. It is profoundly known that Ni-based catalyst are excellent in TCD process<sup>28, 29</sup>. Takenaka et al.<sup>30</sup> studied the effect of catalytic supports (MgO, Al<sub>2</sub>O<sub>3</sub>, SiO<sub>2</sub>, TiO<sub>2</sub>, ZrO<sub>2</sub>, MgO.SiO<sub>2</sub>, Al<sub>2</sub>O<sub>3</sub>.SiO<sub>2</sub>, H<sup>+</sup>-ZSM-5, and so on) for Ni for producing hydrogen and carbon nanofibers by TCD process and concluded SiO<sub>2</sub> as the most efficient catalyst support. However, we have concentrated to study on SiO<sub>2</sub> as a support

to design a nano-structured catalyst with a longer life and higher activity.

In the present study, we report a new approach to prepare nano-structured n-Ni/SiO<sub>2</sub> catalysts with a simple room temperature processing named co-precipitation cum modified Stöber method; a continuous process avoiding application of higher temperature calcination before supporting metal with SiO<sub>2</sub>, irrespective of pre-experimented methods<sup>1, 31</sup>. And hence, we have been emphasizing to produce fine nanoparticles avoiding n-NiO particle agglomeration when performing calcination before supporting with SiO<sub>2</sub>. Onwards, we have conducted TCD in a pilot plant to study its stability and activity at different temperature with time on stream. We found that the as-prepared n-Ni/SiO<sub>2</sub> catalyst exhibit high catalytic stability in comparison with the traditional Ni/SiO<sub>2</sub> catalysts. Furthermore, the co-precipitation cum modified Stöber method was extended to other metals like iron and cobalt with same SiO<sub>2</sub> support and conducted preliminary activity inspection. Investigation of physicochemical properties of the catalyst done by means of N<sub>2</sub> adsorption-desorption measurement, X-ray diffraction (XRD), high resolution transmission electron microscopy (HRTEM), hydrogen temperature programmed reduction (H<sub>2</sub>-TPR), ammonia temperature programmed desorption (NH<sub>3</sub>-TPD) and thermogravimetric (TGA) analysis. In addition, the characterization of the formed nano carbon fibers and tubes at various temperatures was explained with help of HRTEM and XRD.

## Experimental Section

Co-precipitation cum modified Stöber method is a compiling of M-OH precipitation and SiO<sub>2</sub> support formation over precipitated M-OH consecutively. Preliminarily, nano-sized M-OH containing suspension was prepared by treating metal nitrate with ammonia solution at room temperature, which prevent agglomeration of metal oxides at comparatively higher temperature. The SiO<sub>2</sub> support was fabricated through hydrolysis of a mixture of tetraethylorthosilicate (TEOS) and Octadecyl trimethoxy silane (C18TMS) with aqueous solution of ammonia<sup>32</sup>.

## Chemicals used

Nickel (II) Nitrate Hexahydrate (Ni(NO<sub>3</sub>)<sub>2</sub>.6H<sub>2</sub>O), Cobalt (II) Nitrate Hexahydrate (Co(NO<sub>3</sub>)<sub>2</sub>.6H<sub>2</sub>O) and Octadecyl trimethoxy silane (C18TMS) were purchased from Acros Organics. Iron (III) nitrate nonahydrate (Fe(NO<sub>3</sub>)<sub>3</sub>.9H<sub>2</sub>O) and Tetraethyl orthosilicate (TEOS) were purchased from Aldrich and used as such. NH<sub>3</sub> solution and ethanol bought from R&M solutions. 99.999% hydrogen, 99.995% methane and 99.99% nitrogen were purchased from Linde Malaysia Sdn. Bhd.

## Preparation of nano-Ni/SiO<sub>2</sub> catalyst

Sonicate 200ml of 0.1 molar Ni(NO<sub>3</sub>)<sub>2</sub>.6H<sub>2</sub>O solution for 5 minutes and add 6ml of 30%NH<sub>3</sub> solution drop by drop while sonicating. Allow the solution to precipitate metal hydroxide under sonication for 1 hour. Stir the resulting suspension for another one hour over a magnetic stirrer at room temperature. Then, centrifuge the solution at 4000RPM for 30 minutes and wash the precipitate two times with deionized water and one time with ethanol. Transfer the product to 100ml of ethanol and stir for 15 hours with magnet. Sonicate the resulting suspension for 10 minutes and add 4ml of 8M NH<sub>3</sub> solution to make the suspension basic. Add 0.4 mL of TEOS and 0.4ml of C18TMS simultaneously to the dispersion under sonication, and then the resulting mixture sonicate for further 60 minutes at room temperature. Stir the solution for further 5 hours over a magnetic stirrer. Separate the precipitate by centrifugation and dry in an oven at 100°C for 15 hours. Calcinate at 450°C for 3 hours to produce n-NiO/SiO<sub>2</sub> (0.02) nano-structures. The produced nano-catalyst treated with 30%H<sub>2</sub> at 550°C to reduce NiO before its activity examination and named n-Ni/SiO<sub>2</sub> (0.02). Hence, 0.02 mol of Ni precursor was used for its preparation. Nano-structures with higher nickel precursor concentrations like 0.04 mol named n-Ni/SiO<sub>2</sub>(0.04) and 0.06 mol named n-Ni/SiO<sub>2</sub>(0.06) were also prepared. In order to prepare n-NiO particle, the suspension after 15 hours of stirring (before adding silica precursors in the above procedure) was evaporated at 100°C and calcinated at 350°C.

Preparation method was extended to other metals like Fe and Co with  $\text{Fe}(\text{NO}_3)_3 \cdot 9\text{H}_2\text{O}$  and  $\text{Co}(\text{NO}_3)_2 \cdot 6\text{H}_2\text{O}$  precursors, respectively.

## Characterization

### XRD

X-ray diffraction (XRD) patterns of the fresh and spent catalysts were collected at room temperature in PANalytical diffractometer to determine the crystal phase and structure of the metal oxides. The evaluation of the diffractograms was made by X'pert HighScore software. Diffraction patterns of the samples were recorded with a Rigaku Miniflex with Cu K $\alpha$  radiation with a generator voltage and a current of 45 kV and 40 mA, respectively. The intensity was measured by step scanning in the 2 $\theta$  range of 8–80° with a step of 0.026° and a scan rate of 0.0445°/s. The average crystallite size was obtained using the global Scherrer equation as follows:

$$D_{\text{avg}} = \frac{0.9\lambda}{\beta \cos\theta} \left( \frac{180}{\pi} \right) \quad (2)$$

In Eq. (2), the average crystallite size, peak length, line broadening full width at half-maxima after subtracting the instrumental line broadening (in radians), and the Bragg's angle are expressed as  $D_{\text{avg}}$  (nm),  $\lambda$  (1.54056 Å),  $\beta$ , and  $2\theta$ , respectively. 0.9 is the Scherrer constant.

### Nitrogen adsorption-desorption analysis

Nitrogen adsorption-desorption measurements (BET method) were performed at liquid nitrogen temperature (-196°C) with an autosorb BET apparatus, Micromeritics ASAP 2020, surface area and porosity analyzer to determine the surface area, pore size distribution and structure, pore volume and the mean particle size. Before each measurement, the samples were first degassed at 180°C for 4 hours and thereafter kept at liquid nitrogen temperature to adsorb nitrogen. The surface area was determined according to the standard Brunaur–Emmett–Teller (BET) method in a relative pressure range of 0.04–0.2 and the total volume was evaluated from the amount of adsorbed N<sub>2</sub> at a relative pressure (P/P<sub>0</sub>) of about 0.98. The pore diameter distributions were

calculated based on the desorption isotherms by the Barrett–Joyner–Halenda (BJH) method.

### HRTEM-EDX analysis

The morphological structure and diameter distribution of the catalysts and produced carbon nanomaterials were estimated with high resolution transmission electron microscopy (HRTEM) by using a FEI Tecnai™, controlled at an accelerating voltage of 200 keV. The required specimens were fabricated by ultrasonic dispersion in ethanol with a drop of the resulting suspension evaporated onto an electron carbon-supported 300 mesh copper grid.

### Temperature-programmed reduction (H<sub>2</sub>-TPR)

Temperature-programmed reduction measurements were carried out using a Micromeritics TPD/TPR 2720 analyzer. Typically, 0.03 g of catalyst sample was placed in a U-tube holder and the sample was first cleaned at 130°C for 60 minutes by flushing with helium gas. Upon cleaning process, the reductive gas mixture consisting of 5% hydrogen balanced with nitrogen at a flow rate of 20 mL/min streamed through the sample. The sample was heated from 175°C to 750°C to obtain the TPR profiles of the sample.

### Temperature-programmed desorption (NH<sub>3</sub>-TPD)

A Micromeritics TPD/TPR 2720 analyzer was used to characterize how NH<sub>3</sub> molecules are strongly conjugated to the acid sites qualitatively. Firstly, 0.03 g of catalyst was heated under helium with a flow rate of 20 mL/min. Increase the temperature of the system to 600°C with a temperature ramp of 10°C/min and let the system stay for 60 min. Then, a helium flow of 20 mL/min was purged while cooling down the catalyst bed to 225°C. Thereafter, 10% ammonia balanced with helium was streamed on the samples for 30 min with a flow of 20mL/min to effectively adsorb on the catalyst. Afterwards, physisorbed elements from the samples were removed by purging helium for another one hour. The chromatograms were recorded from the signal processing of thermal conductivity detector using the temperature ramp of 10°C/min from 75°C to 625°C.

## Thermogravimetric analysis (TGA)

The thermogravimetric analysis (TGA) analysis of each catalyst was performed with Diamond TGA (PerkinElmer) instrument. Quantitative degradation of catalyst was analyzed by heating catalyst from 30°C to 700°C at a rate of 10°C/min under the synthetic air flow at 200 ml/min. Then, the samples were kept at final temperature for 20 min.

## Catalytic activity

### Experimental setup

Catalytic tests were carried out in a fixed bed reactor of dimension 6.03cm outer diameter, 0.87cm wall thickness and 120cm height constructed with stainless steel material (SS310S). A quartz tube (3.56cm internal diameter, 4 cm outer diameter, and 120 cm height), obtained from Technical Glass Products (Painesville, USA), was placed inside the reactor in order to avoid interaction of feed gas with stainless steel. A quartz frit (3.5 cm diameter, 0.3 cm in thickness, and 150 $\mu$ m to 200 $\mu$ m porosity) placed at the middle of the quartz tube was used as catalyst bed. Temperature was supplied with a vertically mounted, three-zone tube furnace (model TVS 12/600, Carbolite, UK). Temperature measurements were recorded by using two K-type thermocouples (1/16 in diameter, Omega, USA). The first thermocouple was fixed on the exterior surface of the stainless steel tube. The second thermocouple was inserted into the quartz tube momentarily for calibration and removed afterward from the quartz tube prior to testing because its internal copper material could affect the TCD of methane<sup>33</sup>. In addition, pressure and temperature indicators were placed at different locations to control the operating conditions. A two-differential pressure transducer (0" H<sub>2</sub>O to 4" H<sub>2</sub>O) was supplied by Sensocon to measure the pressure drop across the reactor. Mass flow controllers (Dwyer, USA) in the range of 0-2 L/min were used to control the gas flow rates. The outflow gas was then cooled down at room temperature by means of an air cooler. Solid particles that had sizes greater than 2 nm and high molecular weight components were separated using two filters (38 M membrane, Avenger, USA). A

calibrated Rosemount Analytical X-STREAM (UK) was used as an online analyzer to compute the mole percentage of methane and hydrogen.

### Temperature programmed methane decomposition

1gm of catalyst was homogeneously distributed over catalyst bed and purge nitrogen for 30 minutes to clean the furnace and catalyst at flow of 1L/min. Increase the bed temperature to 550°C with a ramp of 20°C/min and pass 30%H<sub>2</sub> in N<sub>2</sub> feed for 2.5 hours to reduce the metal oxide catalyst to its metallic form. Then, decrease the furnace temperature to 25°C under N<sub>2</sub> flow by air cooler. Pass 99.995% methane with a flow rate of 0.64L/min for temperature programmed decomposition from 200°C to 900°C with ramp of 5°C/min.

### Isothermal methane decomposition

Catalyst bed was uniformly covered with 0.5g of catalyst. Pure nitrogen was passed for 30 minutes in order to clean the furnace at flow rate of 1L/min. Then, system temperature was increased to 550°C with a ramp of 20°C/min. Reduction of catalyst was conducted at 550°C by passing 30%H<sub>2</sub> in N<sub>2</sub> feed for 2.5 hours. Then, increase/decrease the temperature to reaction temperature under N<sub>2</sub> flow, accordingly. Once destination temperature reached, N<sub>2</sub> flow was replaced with 99.995% methane with a flow rate of 0.64L/min for evaluating methane conversion at isothermal condition. Influence of flow rate on hydrogen production were analyzed at 550°C with various flow rate.

## Results and discussion

### Production of n-Ni/SiO<sub>2</sub> nano-catalyst

Fine nano-structured Ni/SiO<sub>2</sub> were synthesized by co-precipitation cum modified Stöber method. Stöber method was presented in order to safeguard nano metal active phase with SiO<sub>2</sub> like inert materials. There was no surfactants was used in our method and SiO<sub>2</sub> formation reaction was conducted in alcoholic medium avoiding water content. Hence, water content may hasten hydrolysis process which results in the establishment of particles agglomeration and leave free metal and SiO<sub>2</sub>

particles<sup>34, 35</sup>. Furthermore, free n-NiO particles are nearly eliminated in the final product by increasing its quantity. The overall process constituted with different stages as follows. i) Precipitation of NiOH nanoparticle form precursor  $\text{Ni}(\text{NO}_3)_2 \cdot 6\text{H}_2\text{O}$  with  $\text{NH}_3$  solution; ii) The produced fine nanoparticles were directly supported with  $\text{SiO}_2$  by the Stöber method<sup>32</sup>.  $\text{SiO}_2$  protection was developed uniformly over dispersed NiOH particles with a mixture of C18TMS and TEOS. C18TMS was added to the reaction mixture in the sense of increasing the porosity of  $\text{SiO}_2$ . iii) Porosity enhancement on  $\text{SiO}_2$  was done by calcination under air at 450°C and reduction at 550°C, which remove all organic moieties and convert metal oxides to metal. It was reported that 450°C is insignificant for aggregation of metal oxide nanoparticles<sup>36</sup>. While, the added C18TMS helps to sparse silica polymerization and produces more pores inside the silica network after calcination. Those heat treatments did not lead to metal particle agglomeration because of the efficacious prevention of silica coating. When the particle size of n-NiO were increased to giant figures (48.02 nm to 12933.53nm) on reduction treatment,  $\text{SiO}_2$  supported structures maintained its mean size with a minor increase like 32.19nm to 52.78nm (detailed BET results furnished in Table 2). Different precursor quantities were experimented in order to enhance the yield without effecting its structure and properties. The major challenge observed in nano-compound processing is the quantity of the product which is tackled in our method resulting in higher yield. However, the quality of the product in terms activity (see Fig. S4) and particle size distribution found intact (see HRTEM images; Fig. 5, Fig. S2 and S3). Consequently, the method was extended to different active metals like cobalt and iron. A series of characterization were conducted to enlighten the characteristics of nanostructures. Furthermore, activity and stability were studied for TCD at various temperature and methane feed flow rate in a fixed bed pilot plant.

## Characterization of the catalyst before TCD

### XRD

The degree of structural order, longevity of catalyst and catalyst activity in fresh and deactivated

samples are usually related with the apparent size of the crystallites determined by X-ray diffraction (XRD). Fig. 2 shows the XRD patterns for calcined and reduced (550°C for 2.5 hours in 30%  $\text{H}_2/\text{N}_2$ ) n-Ni and n-Ni/ $\text{SiO}_2$  nanostructures with different precursor concentration. All XRD patterns have three major diffraction peaks, which respectively correspond to (111), (200) and (220) reflections of the solid. The crystalline size corresponds to each peak according to Scherrer equation is furnished in Table 1. The diffraction peaks located at  $2\theta = 44.52^\circ$ ,  $51.87^\circ$  and  $76.40^\circ$  corresponds to the d-spacing of 2.033 Å, 1.761 Å and 1.245 Å, respectively for completely reduced n-NiO as shown in Fig. 2(a). The positions of the diffraction peaks in the sample are in good agreement with those given in JCPDS NO: 98-064-6092 for nickel phase. It is observed that the addition of  $\text{SiO}_2$  diminishes the intensities of XRD peaks corresponds to NiO, showing a reduction of the structural ordering. It is obvious that the reduction with 30% hydrogen for 2.5 hours at 550°C was sufficient to convert calcinated n-NiO to n-Ni metallic phases. Hence, XRD pattern shows metallic Ni phase only (Fig 2 (a)). While, n-Ni/ $\text{SiO}_2$  structures exhibit both metallic and metal oxide phases (Fig 2 (b-d)) even after  $\text{H}_2$  treatment which indicates that the reduction treatment is insufficient for n-Ni/ $\text{SiO}_2$  system, supporting previously conducted experimental reports<sup>37</sup>. Even though, the NiO phases can be seen verily abridged in the reduced n-Ni/ $\text{SiO}_2$  XRD pattern (Fig. 2 (b-d)).

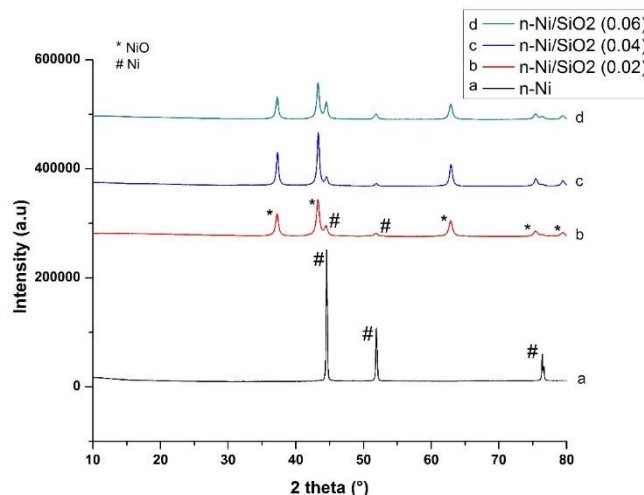


**Fig. 2** XRD patterns of a) n-Ni, b) n-Ni/SiO<sub>2</sub> (0.02), c) n-Ni/SiO<sub>2</sub> (0.04) and d) n-Ni/SiO<sub>2</sub> (0.06). Peaks corresponds to NiO and Ni were indicated.

**Table 1**

Crystallite sizes of n-Ni and n-Ni/SiO<sub>2</sub> nanostructures with different precursor concentration before TCD process from XRD analysis. And crystallite sizes of n-Ni/SiO<sub>2</sub> (0.02) nanostructures after TCD process at different temperature.

| Sample                       | Ni (111) (nm) | Ni (200) (nm) | Ni (220) (nm) | Avg. (nm) |
|------------------------------|---------------|---------------|---------------|-----------|
| n-Ni                         | 61.18         | 78.71         | 72.06         | 70.65     |
| n-Ni/SiO <sub>2</sub> (0.02) | 28.54         | 43.84         | 29.26         | 33.88     |
| n-Ni/SiO <sub>2</sub> (0.04) | 33.97         | 31.75         | 47.55         | 37.75     |
| n-Ni/SiO <sub>2</sub> (0.06) | 31.14         | 29.11         | 29.24         | 29.83     |
| TCD-600                      | 70.14         | 45.11         | 25.84         | 47.03     |
| TCD-550                      | 70.15         | 25.77         | 29.45         | 41.79     |
| TCD-500                      | 26.98         | 51.55         | 29.49         | 36        |
| TCD-475                      | 26.97         | 72.11         | 51.58         | 50.22     |

In the activity side, it is not influencing TCD process as methane itself is acting as an excellent reducing agent and hence there is no NiO phases were detected in XRD patterns after TCD (Fig. 10). Moreover, existing NiO phases are supposed to interact with porous silicate support result in accomplishment of complex catalysis environment which likely leads to a more stable reaction course during the TCD of methane. However, the average crystallite size of the n-Ni and n-Ni/SiO<sub>2</sub> calculated using global Scherrer equation (furnished in Table 1) evidently close to the mean particle size obtained from BET analysis (furnished in Table 2). The mean crystallite sizes furnished in Table 1 clearly manifested that the protection of SiO<sub>2</sub> over n-NiO clearly prevent agglomeration. Hence, average crystallite size of n-NiO was 70.65nm is reduced to around half when supported with SiO<sub>2</sub>. One can observe that the intensity and width of reflections of the NiO peaks in the n-Ni/SiO<sub>2</sub> nanostructures changes with precursor's concentration. It may be attributed to the variation of the dispersion happening during silicate formation process as it was accomplished with mixture of TEOS and C18TMS in a basic ethanol solution under sonication. Ultrasonic treatment is supposed to enhance the dispersion, while the fairly higher content of TEOS and C18TMS mixture may reduce such an effect<sup>38</sup>. Hence, the variation in NiO dispersion at different precursor concentration

shows an impact on the intensity and width of reflections of NiO.

### Nitrogen adsorption-desorption measurements

Table 2 furnish the physical characteristics of n-NiO and n-NiO/SiO<sub>2</sub> (0.02). The BET mean particle size of NiO (48.02nm) found contracted after supporting with SiO<sub>2</sub> (32.19nm). This observation illustrate that the support effectively prevent agglomeration of air-sensitive n-NiO particle during heat treatments such as calcination as well as reduction processes. The silica support not only leads to diminution of average particle size, but also increases the overall surface area and porosity. Compared with the naked n-NiO, the n-NiO/SiO<sub>2</sub> samples have higher specific surface areas (Table 2), this is due to the presence of SiO<sub>2</sub> and its porosity. It is found that there is no significant changes were occurred with physical characteristics like particle size (~30nm) or surface area (~95±5m<sup>2</sup>/g) as increasing the precursor concentration. Fig. 3 depicts the N<sub>2</sub> adsorption-desorption isotherms of n-NiO and n-NiO/SiO<sub>2</sub> (0.02). The pore diameter distributions of the samples considered from desorption division of the isotherm by using BJH method and the corresponding data are shown in Fig. 3 and Table 2. Furthermore, the N<sub>2</sub> adsorption-desorption isotherms and BJH pore diameter distribution of n-NiO/SiO<sub>2</sub> (0.04) and n-NiO/SiO<sub>2</sub> (0.06) are displayed in Fig. S1. It can be seen that the pore sizes

are mainly distributed below 30 nm in both n-NiO and n-NiO/SiO<sub>2</sub>. The pores observed in the mesoporous and macroporous region with a pore size of 50 nm to 150 nm can be attributed to the

**Table 2**

Physical characteristics of n-NiO, n-NiO/SiO<sub>2</sub> (0.02), n-NiO/SiO<sub>2</sub> (0.04) and n-NiO/SiO<sub>2</sub> (0.06) from N<sub>2</sub> adsorption-desorption analysis.

| Catalyst                      | Single point SA <sup>a</sup> (m <sup>2</sup> /g) | BET SA (m <sup>2</sup> /g) | Micropore area <sup>b</sup> (m <sup>2</sup> /g) | Mesopore + external area <sup>c</sup> (m <sup>2</sup> /g) | Micropore volume <sup>d</sup> (cm <sup>3</sup> /g) | Total pore volume <sup>e</sup> (cm <sup>3</sup> /g) | Mesoporous volume (cm <sup>3</sup> /g) | BET pore size (nm) | Mean particle size (nm) |
|-------------------------------|--|----------------------------|---|---|--|---|--|--------------------|-------------------------|
| n-NiO                         | 62.22  | 62.46                      | 5.17  | 57.28   | 0.0020   | 0.2499  | 0.2479                                 | 16.274             | 48.02                   |
| n-NiO/SiO <sub>2</sub> (0.02) | 91.50  | 93.18                      | 5.17  | 88.01   | 0.0024   | 0.2301  | 0.2277                                 | 9.987              | 32.19                   |
| n-NiO/SiO <sub>2</sub> (0.04) | 90.62  | 92.53                      | 6.24  | 86.28   | 0.0030   | 0.2036  | 0.2006                                 | 8.901              | 32.42                   |
| n-NiO/SiO <sub>2</sub> (0.06) | 102.64   | 104.6                      | 6.47  | 98.21   | 0.0031   | 0.2148  | 0.2117                                 | 8.235              | 28.65                   |

<sup>a</sup> Represents the values calculated at a relative pressure (P/P<sub>0</sub>) of N<sub>2</sub> equal to 0.301.

<sup>b-d</sup> Represents the values calculated from t-plot method.

<sup>e</sup> Represents the total pore volume evaluated from nitrogen uptake at a relative pressure (P/P<sub>0</sub>) of N<sub>2</sub> equal to 0.98.

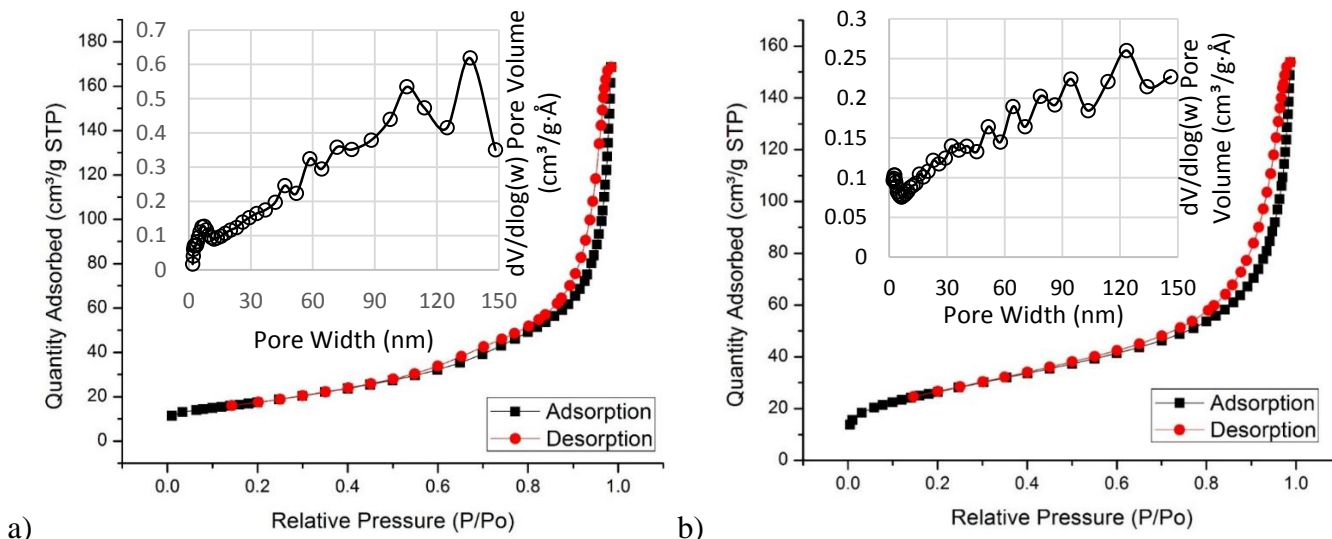


**Fig. 3** Loops of N<sub>2</sub>-adsorption–desorption isotherms of (a) n-NiO and (b) n-NiO/SiO<sub>2</sub> (0.02) catalyst. The inset plot shows the pore diameter distributions calculated with Barrett–Joyner–Halenda (BJH) method.

### HRTEM-EDX

Fig. 4 and 5 shows the HRTEM images, particle size distribution measured with ImageJ software and EDX elemental mapping of n-NiO and n-NiO/SiO<sub>2</sub> (0.02) nanocatalysts, respectively. Most of the unsupported n-NiO exhibit particle size >40. While, the diameters of NiO active phase in SiO<sub>2</sub> supported sample were found in the range of 0–50 nm and very

formation of voids due to inter-nanoparticles in contact.

less particle can be seen above 50 nm. Particle size distribution histograms of n-NiO (Fig. 4b) and n-NiO/SiO<sub>2</sub> (0.02) (Fig. 5b) supporting the BET analysis report (Table 2) and H<sub>2</sub>-TPR results (Fig. 6a). It can be speculate that the structure of particles are not uniform and n-NiO were found aggregated in some location to form multiplicated structure. This agglomeration results in structural intricacy leads to difficulties in reduction, supporting elongation of

$H_2$ -TPR curve to slightly higher temperature (Fig. 6a). The active n-NiO/SiO<sub>2</sub> samples have fairly uniform average particle size at lower and higher precursor concentration. While, the particle size distribution of n-NiO/SiO<sub>2</sub> prepared with higher precursor concentration (Fig. S2 and S3) shows slightly higher percentage of particles with size >50nm, compared to that of n-Ni/SiO<sub>2</sub> (0.02). It can be credited to the particle agglomeration because of magnetic properties of n-NiO as increasing its quantity<sup>35</sup>. The particle sizes are not exceeding

100nm in the multiplicated structures even at higher concentration. It is thought that there is little diffusion limitation in such a thin and porous SiO<sub>2</sub> support. The elemental composition were confirmed by EDX analysis and presented in Fig. 4c and 5c. The presence of C and Cu in the EDX mapping can be attributed to the elements in the electron carbon-supported 300 mesh copper grid used for HRTEM analysis and those elements were omitted from elemental percentage composition table.

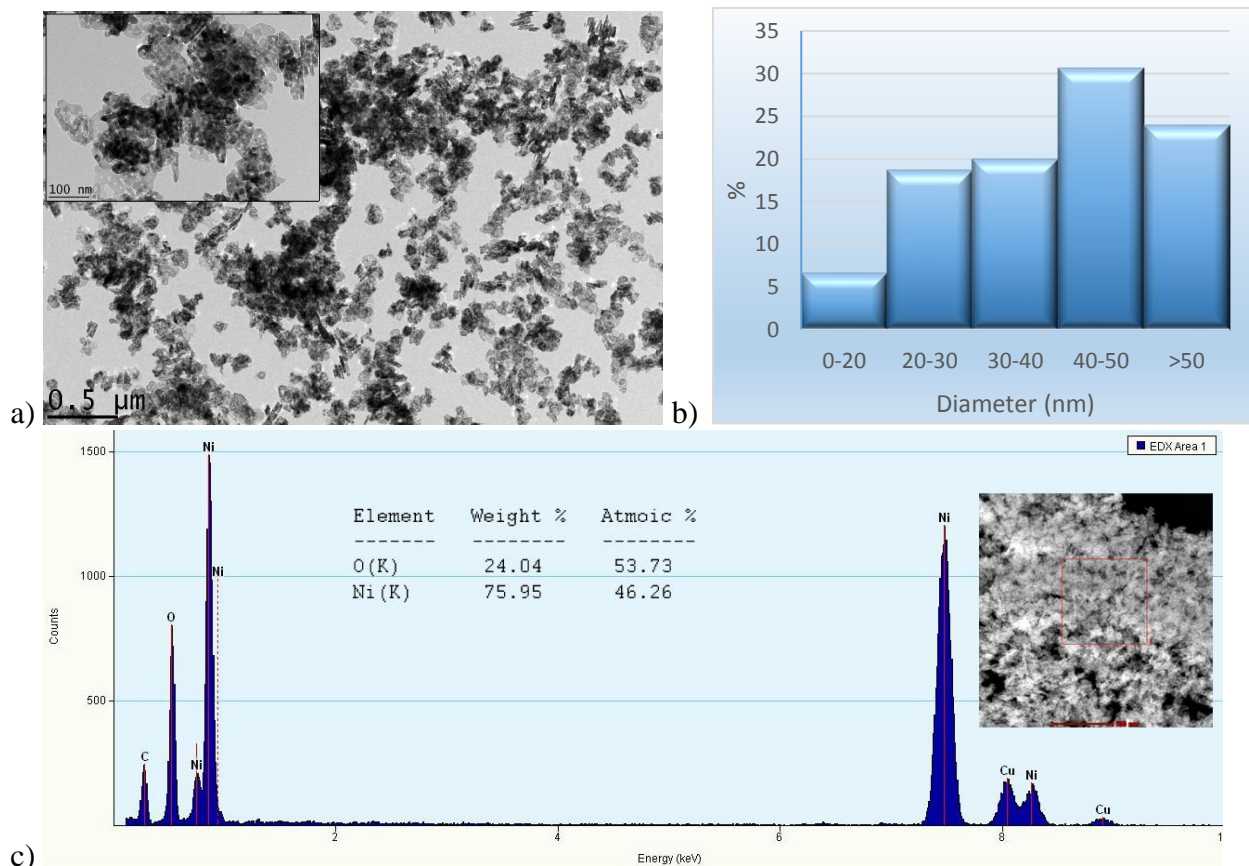


**Fig. 4** a) HRTEM images, b) particle size distribution and c) EDX mapping of n-NiO. 75 nanoparticle were considered to plot particle size distribution histogram. ImageJ software was used to measure particle size.

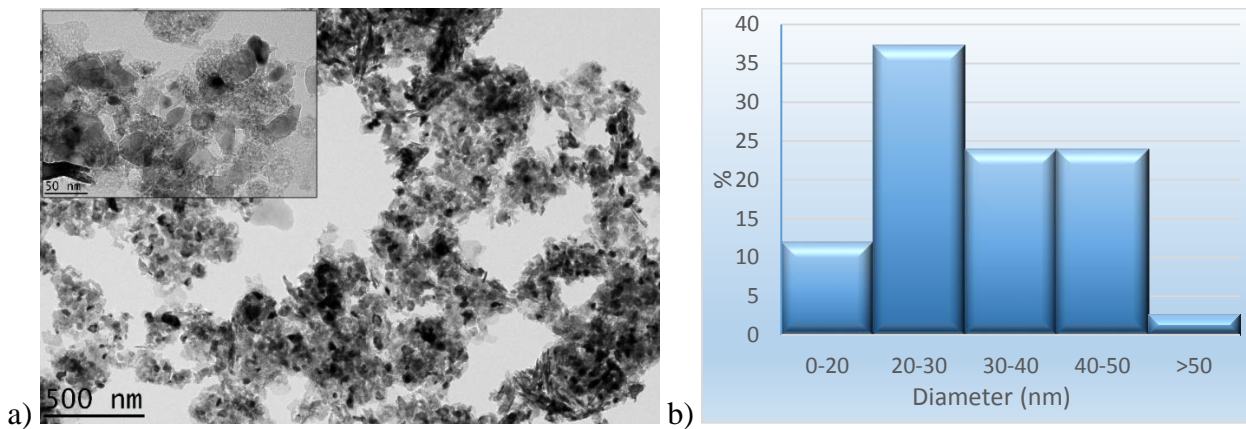


**Fig. 5** a) HRTEM images, b) particle size distribution of n-NiO/SiO<sub>2</sub>(0.02). 75 nanoparticle were considered to plot particle size distribution histogram. ImageJ software was used to measure particle size.

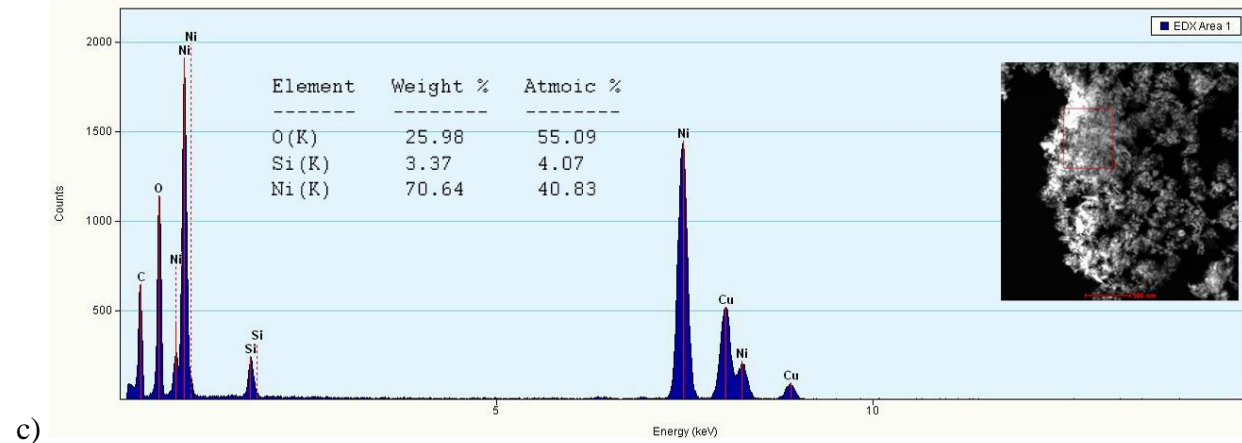
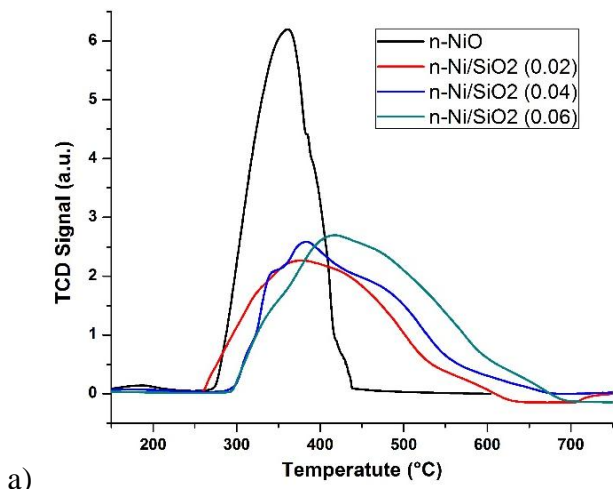
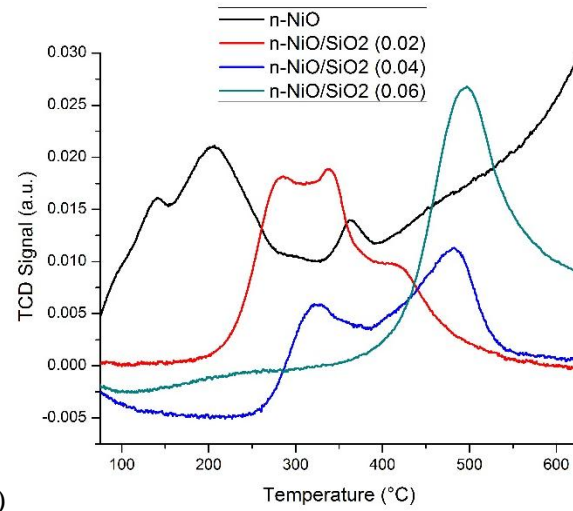


**Fig. 5 c)** EDX mapping of n-NiO/SiO<sub>2</sub>(0.02).

## H<sub>2</sub>-TPR and NH<sub>3</sub>-TPD



a)



b)

**Fig. 6** a) H<sub>2</sub>-TPR and b) NH<sub>3</sub>-TPD profile of n-NiO, n-NiO/SiO<sub>2</sub> (0.02), n-NiO/SiO<sub>2</sub> (0.04) and n-NiO/SiO<sub>2</sub> (0.06).

The H<sub>2</sub>-TPR and NH<sub>3</sub>-TPD profile of n-NiO and n-NiO/SiO<sub>2</sub> with three different nickel precursor concentrations (0.02, 0.04 and 0.06 mole of

$\text{Ni}(\text{NO}_3)_2 \cdot 6\text{H}_2\text{O}$ ) are reported in Fig. 6. Reduction of stoichiometric n-NiO exhibit a peak from  $278^\circ\text{C}$  to  $440^\circ\text{C}$  with a maximum at  $360^\circ\text{C}$  in accordance with pre-experimental reports<sup>39</sup>. It is calculated for  $\text{H}_2$ -TPR peak that n-NiO consumed  $282.8 \text{ mL/g}_{\text{cat}}$  of  $\text{H}_2$  for its reduction. n-NiO reinforced with  $\text{SiO}_2$  starts to reduce at the same temperature as n-NiO did, while its reduction was further extended to higher temperature range.  $\text{H}_2$ -TPR profile of n-NiO/ $\text{SiO}_2$  samples exhibit a single peak in between  $280^\circ\text{C}$  and  $700^\circ\text{C}$  can be assigned to the complete reduction of NiO species, supporting previous records<sup>31, 40</sup>. The  $\text{H}_2$ -TPR quantify a  $\text{H}_2$  conception of  $330.3 \text{ mL/g}_{\text{cat}}$  for n-NiO/ $\text{SiO}_2$  (0.06). While, n-NiO/ $\text{SiO}_2$  (0.02) and n-NiO/ $\text{SiO}_2$  (0.04) taken  $250.7 \text{ mL/g}_{\text{cat}}$  and  $277.4 \text{ mL/g}_{\text{cat}}$   $\text{H}_2$  for complete reduction, respectively. It is apparent to note that the n-NiO/ $\text{SiO}_2$  could be reduced at temperature range of  $300$ - $550^\circ\text{C}$  in agreement with previous observation on Ni-based compounds<sup>41</sup>. There is only one reduction peak were observed with n-NiO/ $\text{SiO}_2$  catalysts reveal a homogenous interaction between metal and support. It was observed that the metal-support interaction is dependent upon metal constitution and the particle size distribution differs from that in the supported systems<sup>38</sup>. n-Ni/ $\text{SiO}_2$  nano-structured catalysts unveil broader  $\text{H}_2$ -TPR peak irrespective of the conventional metal supported catalysts<sup>42</sup>. Hence, it is difficult to reduce nano-material produced by co-precipitation cum modified Stöber method compared to the conventionally supported Ni/ $\text{SiO}_2$  catalysts because of the much stronger interaction between metal and support<sup>31</sup>. Furthermore, the alteration of the reduction peak towards a higher value can be attributed to the presence of some higher sized n-NiO. Hence, one can note that the  $\text{H}_2$ -TPR peak of n-NiO/ $\text{SiO}_2$  (0.04) slightly extended to higher temperature values compared to that of n-NiO/ $\text{SiO}_2$  (0.02). Similarly, n-NiO/ $\text{SiO}_2$  (0.06) has a broader peak than that of n-NiO/ $\text{SiO}_2$  (0.04). However, the denser  $\text{SiO}_2$  support may cause difficulty in hydrogen diffusion and n-NiO reduction.

Fig. 6b show the  $\text{NH}_3$ -TPD profile for determining the number of surface Ni sites which adsorb  $\text{NH}_3$  per unit mass of catalyst. Because of the diffusional limitations, the acid sites computed with  $\text{NH}_3$ -TPD is not very accurate like the actual acidity strength

measured with quantitative measurements<sup>43</sup>. Hence,  $\text{NH}_3$ -TPD is not commonly accepted as a reliable characterization method for computing the precise quantity of acid sites. While,  $\text{NH}_3$ -TPD can provide a qualitative indication of the conjugation intensity of  $\text{NH}_3$  molecule with acid cites. As shown in Fig.6b, the  $\text{NH}_3$ -TPD curves shows that, the acidity cites increase as increasing the precursor concentrations. While, n-NiO reveals a week interaction of  $\text{NH}_3$  with acid cites with peaks from  $100^\circ\text{C}$  to  $255^\circ\text{C}$ . However, desorption chromatograms of n-NiO/ $\text{SiO}_2$  catalysts start from above  $200^\circ\text{C}$  only, indicate the occurrence of more strong acid cites after supporting n-NiO with  $\text{SiO}_2$ .

### Catalytic methane decomposition

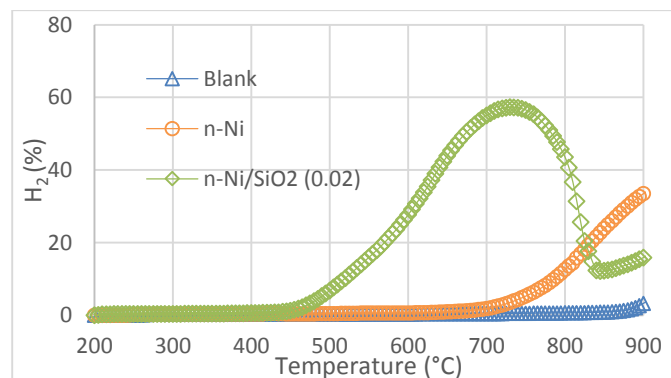


**Fig. 7** Temperature programmed methane decomposition over 1g of n-Ni and n-Ni/ $\text{SiO}_2$  (0.02) catalyst. Temperature range  $200$ - $900^\circ\text{C}$ , flow rate  $0.64\text{L/min}$ .

Temperature programmed methane decomposition were carried out as preliminary experiments in order to determine the temperature ranges where the n-Ni and n-Ni/ $\text{SiO}_2$  (0.02) catalysts were active for TCD. The results are shown in Fig. 7. The temperature programed methane decomposition results reveal that the activity of n-Ni starts above  $700^\circ\text{C}$  only, while n-Ni/ $\text{SiO}_2$  (0.02) is really active from  $450^\circ\text{C}$  to  $\sim 700^\circ\text{C}$ . Hence, n-Ni/ $\text{SiO}_2$  (0.02) catalyst having activity in the comfortable temperature range has been considered for further isothermal studies.

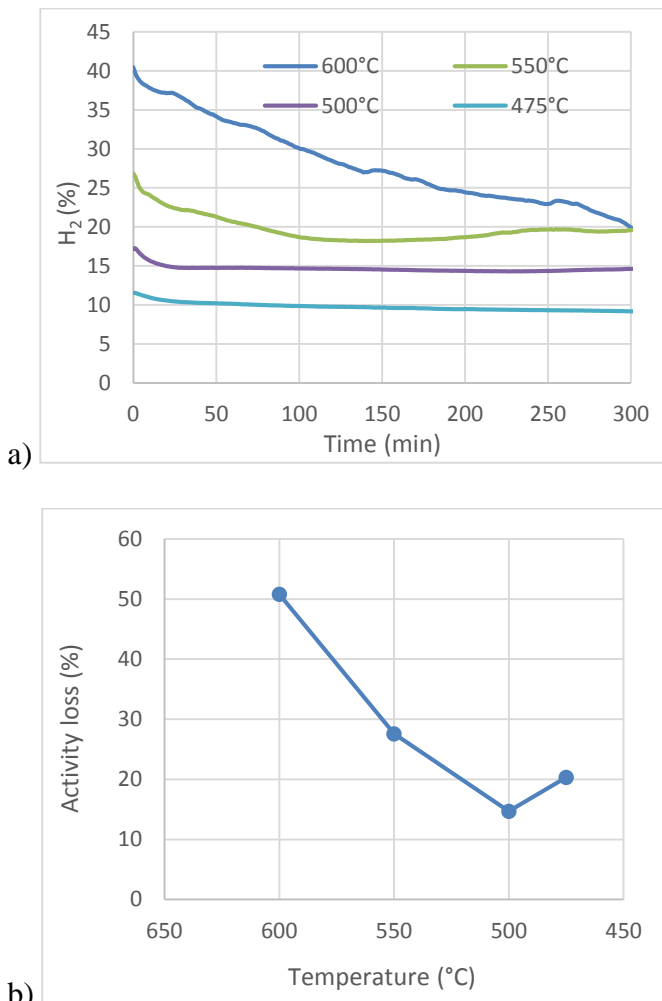


Fig. 8 (a) Isothermal methane decomposition over n-Ni/SiO<sub>2</sub> (0.02) catalyst at different temperature. Flow rate = 0.64 L min<sup>-1</sup> and catalyst weight = 0.5 gm. (b) Activity loss in percentage at each temperature after 5 h of activity examination.

Based on the results from temperature programmed methane decomposition, it was decided to carry out the isothermal catalytic trials in the temperature range of 475–600°C over n-Ni/SiO<sub>2</sub> (0.02) catalyst. Fig. 8a shows the changes in hydrogen production percentage with time on stream for the TCD over n-Ni/SiO<sub>2</sub> (0.02) catalyst at 475–600°C. The experiments were conducted to evaluate activity steadiness of nano-structured catalyst materials as well as its ability to tolerate higher temperature environments. n-Ni/SiO<sub>2</sub> (0.02) catalysts were evaluated with 99.995% methane. During the entire

### Table 3

Comparison of catalytic activity of previously reported metal catalyst with n-Ni/SiO<sub>2</sub> catalyst. Initial activity and activity at time ‘t’ and deactivation time are listed. Values are taken from reference as such.

process, methane and hydrogen only were detected as a gaseous product according to the equation CH<sub>4</sub> → 2H<sub>2</sub> + C. In general, hydrogen production is high just after the contact of methane with the catalyst and decrease gradually by time. It is found from temperature programmed methane decomposition (Fig. 7) that n-Ni/SiO<sub>2</sub> (0.02) was undergoing fast deactivation after 700°C because of its high temperature sensitivity, supporting previous reports<sup>44</sup>, and hence such high temperature studies were omitted from our analysis. Furthermore, according to Takenaka et al.<sup>44</sup>, Ni-based catalysts are effective for methane decomposition in the temperature range of 400–600°C, but deactivated immediately at temperatures above 600°C. Thermal degradation of the n-NiO/SiO<sub>2</sub> might be occurred above 600°C, could be a reason for a rapid deactivation at higher temperature. Hence, a gradual weight loss was observed in thermogravimetric analysis results of n-NiO/SiO<sub>2</sub> as shown in S5, which may be attributed to their thermal degradataion. While, n-Ni/SiO<sub>2</sub> (0.02) catalyst maintained its activity even after 300 minutes with very low catalytic deactivation rate in the temperature range of 475–600°C. Activity loss of n-Ni/SiO<sub>2</sub> (0.02) catalyst in percentage is displayed in Fig. 8b. The initial catalytic activity became higher and catalytic deactivation rate found increase with increasing decomposition temperature clearly indicating the influence of temperature on TCD. Throughout the experimental duration of 300 min, n-Ni/SiO<sub>2</sub> (0.02) catalyst has shown activity in a wide range between 12 to 40.4% at different temperature, no sharp deactivation was observed at any experimented temperatures, indicating the stable catalytic activity of the catalysts under the experimental conditions. We found that the minimum deactivation was occurred at 500°C. We have extended our examination up to 300 min in order to reveal the stability of nano-structured catalyst. One can see that, our n-Ni/SiO<sub>2</sub> (0.02) catalysts are significantly more active and stable than the naked counterpart as well as those prepared by conventional methods (see Table 3).

| Catalyst   | Reaction parameters |                      |                   | Initial         |                | CH <sub>4</sub> | H <sub>2</sub> | t-time | d  |
|--|---------------------|----------------------|-------------------|-----------------|----------------|-----------------|----------------|--------|----|
|  | T                   | CH <sub>4</sub> Flow | Total flow        | CH <sub>4</sub> | H <sub>2</sub> | at time t       |                |        |    |
| Ni/SiO <sub>2</sub> <sup>48</sup>                  | 650                 | 15 <sup>b</sup>      | --                | 42              | --             | 5               | --             | 4      | -- |
| Ni–Ca/SiO <sub>2</sub> <sup>49</sup>               | 580                 | --                   | 100 <sup>b</sup>  | 39              | --             | 12              | --             | 3      | -- |
| Ni–K/SiO <sub>2</sub> <sup>49</sup>                | 580                 | --                   | 100 <sup>b</sup>  | 40              | --             | 5               | --             | 2.5    | 3  |
| Ni–Fe/SiO <sub>2</sub> <sup>48</sup>               | 650                 | 15 <sup>b</sup>      | --                | 46              | --             | 27              | --             | 4      | -- |
| Ni/MgAl <sub>2</sub> O <sub>4</sub> <sup>50</sup>  | 550                 | --                   | 80 <sup>b</sup>   | 34              | --             | 23              | --             | 3      | 4  |
| Ni–Cu/La <sub>2</sub> O <sub>3</sub> <sup>51</sup> | 600                 | --                   | 110 <sup>c</sup>  | 35              | --             | 60              | --             | 10     | -- |
| n-Ni/SiO <sub>2</sub> (0.02) (this work)           | 600                 | 640 <sup>b</sup>     | 640 <sup>b</sup>  | 57.2            | 40.4           | 79.5            | 19.9           | 5      | -- |
| n-Ni/SiO <sub>2</sub> (0.02) (this work)           | 550                 | 640 <sup>b</sup>     | 640 <sup>b</sup>  | 68.5            | 29.4           | 76.9            | 22.9           | 5      | -- |
| n-Ni/SiO <sub>2</sub> (0.02) (this work)           | 500                 | 640 <sup>b</sup>     | 640 <sup>b</sup>  | 74.4            | 17.2           | 85.3            | 14.6           | 5      | -- |
| n-Ni/SiO <sub>2</sub> (0.02) (this work)           | 475                 | 640 <sup>b</sup>     | 640 <sup>b</sup>  | 90.1            | 11.5           | 90.9            | 9.1            | 5      | -- |
| n-Ni/SiO <sub>2</sub> (0.02) (this work)           | 550                 | 1070 <sup>b</sup>    | 1070 <sup>b</sup> | 72.9            | 25.6           | 84.2            | 15.7           | 2      | -- |
| n-Ni/SiO <sub>2</sub> (0.02) (this work)           | 550                 | 1430 <sup>b</sup>    | 1430 <sup>b</sup> | 78              | 21             | 87.3            | 11.9           | 2      | -- |
| n-Ni/SiO <sub>2</sub> (0.04) (this work)           | 550                 | 640 <sup>b</sup>     | 640 <sup>b</sup>  | 69.4            | 29.3           | 79.8            | 20.1           | 5      | -- |
| n-Ni/SiO <sub>2</sub> (0.06) (this work)           | 550                 | 640 <sup>b</sup>     | 640 <sup>b</sup>  | 72.3            | 27.6           | 79.4            | 20             | 5      | -- |

(T, temperature (°C); F, flow rate (<sup>a</sup>mL/(g<sub>cat</sub>.h)<sup>b</sup>mL/min, <sup>c</sup>NmL/min, unless other units are stated); Conversion (%); t, time (h); d, complete deactivation (h); --, not mentioned in the original paper)

Furthermore, the isothermal methane conversion percentage as well as the activity range indisputably following the temperature range observed in the temperature programmed methane decomposition (Fig. 7). However, it is worth pointing out that in the temperature range of 475°C–600°C, the methane conversions and hydrogen production percentage as well as nanocarbon yield (Fig. 11) over the n-Ni/SiO<sub>2</sub> (0.02) are considerably superior to those reported Ni-based catalyst furnished in Table 3. TCD experiments were conducted over n-Ni/SiO<sub>2</sub> (0.04) and n-Ni/SiO<sub>2</sub> (0.06) at 550°C and compared the results with that of n-Ni/SiO<sub>2</sub> (0.02) as shown in Fig. S3. It can be seen that all those prepared catalyst are behaving in a similar way. Hence, there is no characteristic deprivation with analyzed catalyst were observed as increasing the precursor concentration in a sense to synthesis in large scale method. The results clearly indicate that the examined nano-catalysts are more stable than that of normally supported or naked catalysts. Hence, n-Ni/SiO<sub>2</sub> (0.02) nano-structured catalyst can be assumed as a micro-capsular like reactors<sup>45–47</sup> in which the reactant molecules can get enough space with in the porous support. However, the reactant can get adsorbed within the support through highly porous silicate and accordingly results in higher catalytic activity. The very high stability of n-Ni/SiO<sub>2</sub> catalyst can be attributed effective prevention of silica support from the aggregation of active Ni-phase.

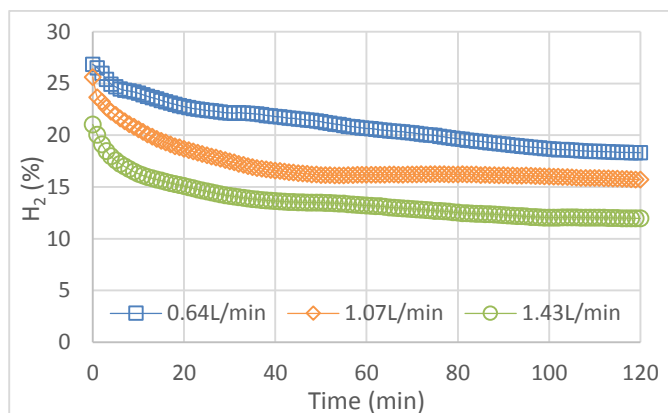
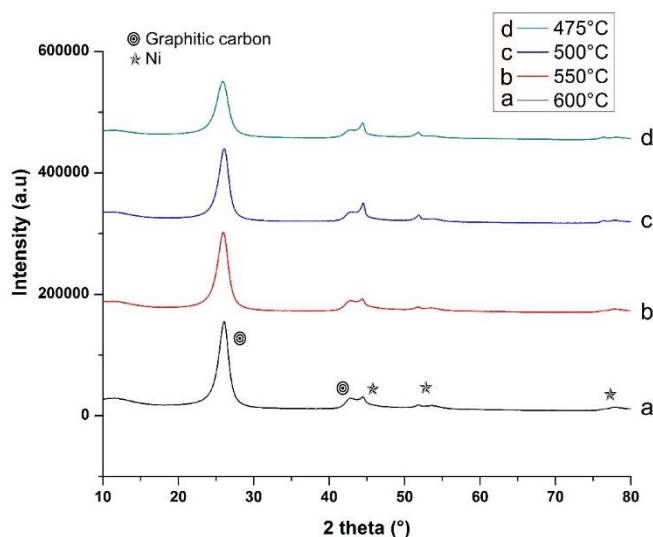


**Fig. 9** Methane decomposition over n-Ni/SiO<sub>2</sub> (0.02) catalyst at different methane feed flow rate. Temperature = 550°C and catalyst weight = 0.5gm.

The effect of methane feed flow rate on hydrogen production in percentage with time on stream is shown in Fig. 9. Flow rates like 0.64L/min, 1.07L/min and 1.43L/min were analyzed at 550°C over 0.5g of catalyst. It is observed from Fig. 9 that initial hydrogen production decreased from 26.8% to 21.04% when flow rate was increased from 0.64L/min to 1.43L/min. It can be speculated that higher methane flow rate results in the lower contact time with catalyst and hence resulted in the lower hydrogen production<sup>15, 52</sup>. Furthermore, it is found that the catalytic deactivation rate is also increases as increasing flow rate.

## Characterization of produced nano-carbon

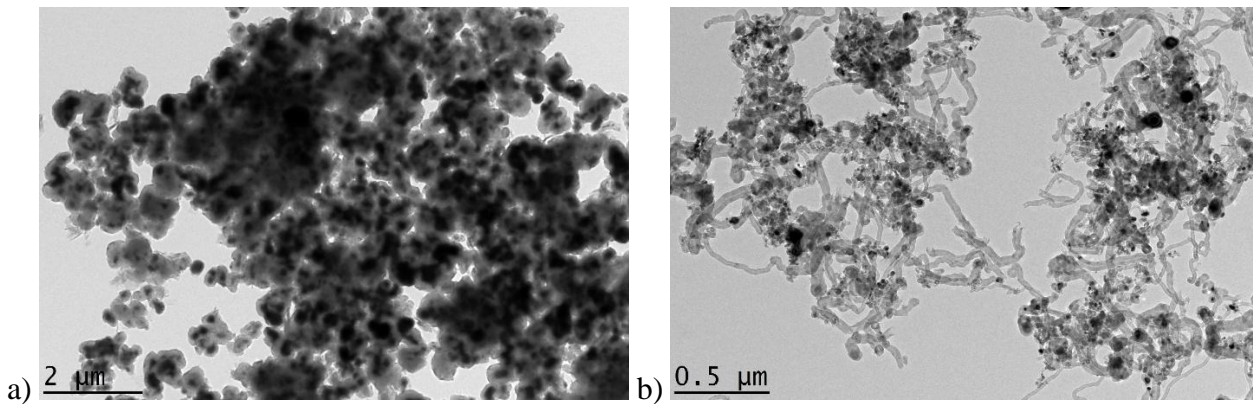
XRD pattern of the produced carbon at 475–600°C are shown in Fig. 10. The diffraction peaks at  $2\theta = 26.26^\circ$  and  $44.45^\circ$  are characteristic to the graphite corresponds to JCPDS No. 98-005-3781. The peaks at  $2\theta = 44.5^\circ$ ,  $51.83^\circ$  and  $76.28^\circ$  corresponds to Ni-phases showing good agreement with JCPDS No. 01-070-1849. It is found that the graphitization intensity of carbon nanofibers got improved as increasing the temperature from 475° to 600°C which is clear from the alteration of  $2\theta$  values corresponds to nanocarbon to higher values in a similar manner to those reported with Ni-supported Y zeolite<sup>53</sup>.



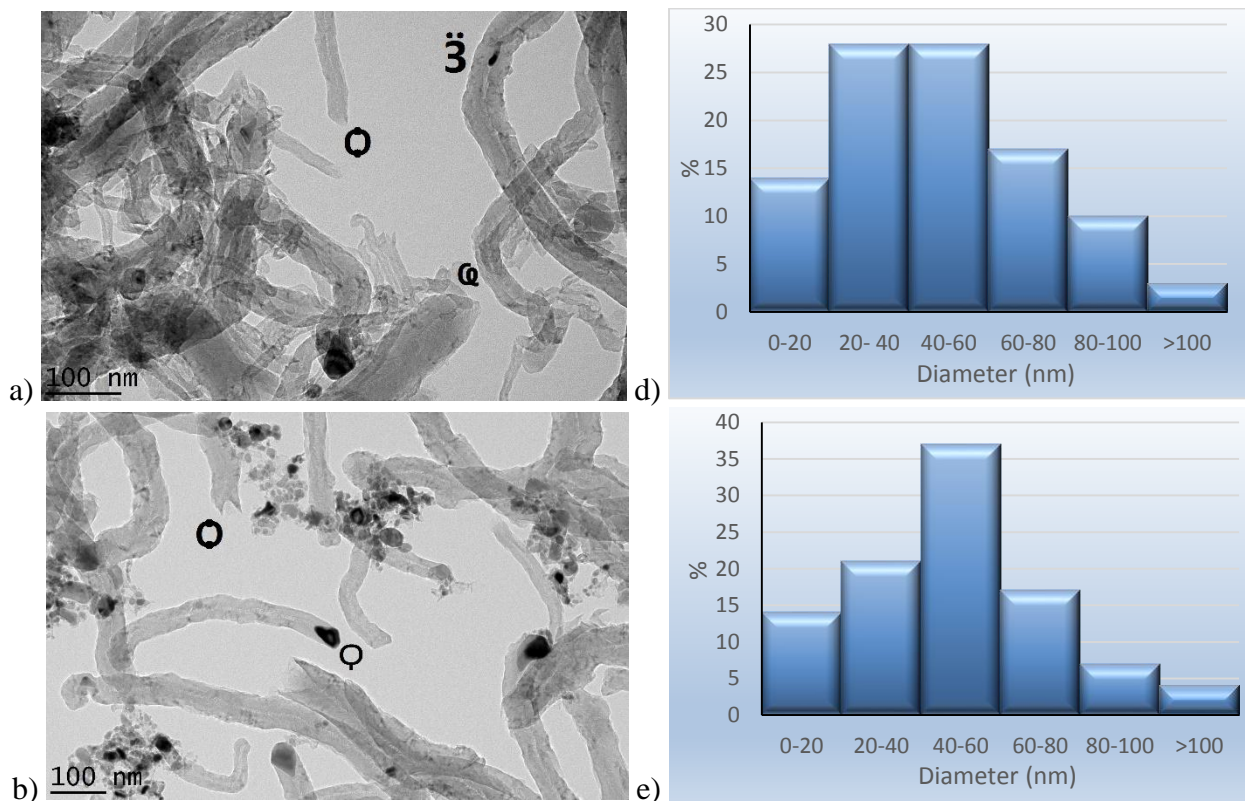
**Fig. 10** XRD patterns of produced nano-carbon over n-Ni/SiO<sub>2</sub> (0.02) at different temperatures.

Peaks corresponds to graphite and Ni were indicated

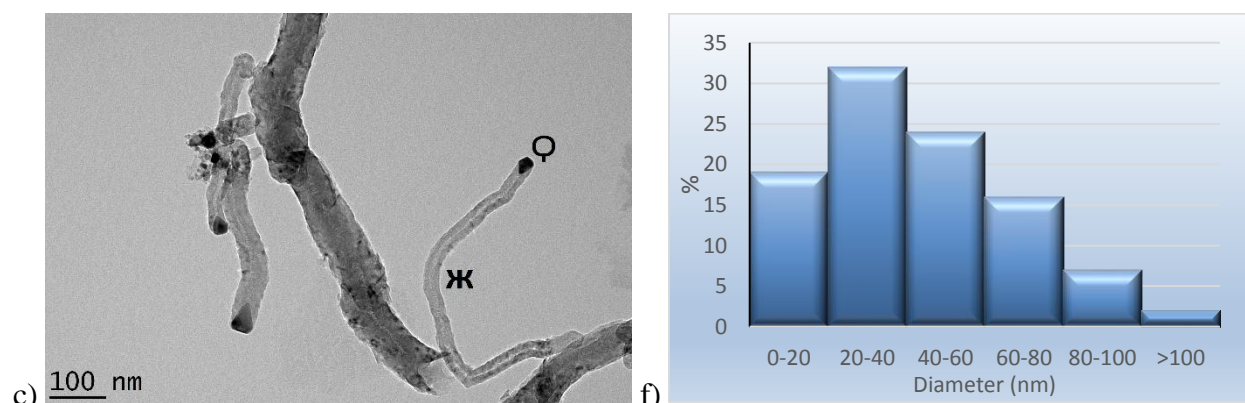
HRTEM images of n-Ni and n-Ni/SiO<sub>2</sub> (0.02) catalyst after temperature programmed methane decomposition are exhibited in Fig. 12. The unsupported n-Ni undergone strong sintering results in the giant agglomerate formation and those are covered by carbon crust which isolates them from the reaction medium and resist further methane decomposition over n-NiO (Fig. 11a). Hence, it was incapable to produce longer carbon nano-filaments as well, supporting our temperature programmed methane decomposition results (Fig. 7). Kim et al.<sup>54</sup> reported the same observation that unsupported nickel powder is not liable for production of nano filaments in hydrocarbon media. While, one can see longer nano-carbon filaments formed over n-Ni/SiO<sub>2</sub> (0.02) catalyst after temperature programmed methane decomposition (Fig. 11b). It can be attributed to the stronger protection of n-NiO after supporting with SiO<sub>2</sub>.



**Fig. 11** HRTEM image of a) n-Ni and b) n-Ni/SiO<sub>2</sub> (0.02) catalyst after TPD analysis.



**Fig. 12** HRTEM images of produced nano carbon and corresponding diameter distribution, a) 600°C and b) 550°C. 75 nano-carbons were considered to plot diameter distribution histogram. ImageJ software was used to measure diameter.



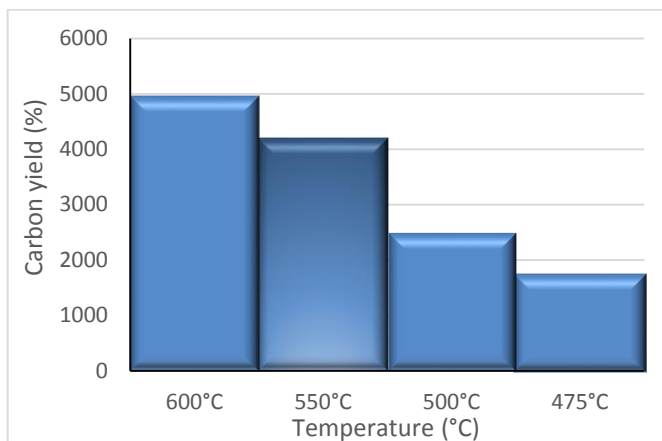
**Fig. 12c** HRTEM images of produced nano carbon produced at 500°C and corresponding diameter distribution. 75 nano-carbons were considered to plot diameter distribution histogram. ImageJ software was used to measure diameter.

Fig. 12 (a-c) exhibit HRTEM images of produced nano carbon by TCD over n-Ni/SiO<sub>2</sub> (0.02) at different temperatures like 600°C, 550°C and 500°C respectively. Accordingly, external diameter distribution of nano-carbon at each temperatures

also unveiled using ImageJ software considering 75 nano-carbon for diameter measurement. Large quantities of nano-carbons were deposited in the catalysts during TCD process. The carbon yield percentage was calculated with the following

equation<sup>55, 56</sup> and the results are depicted in Fig. 13. The carbon yield of the catalysts was evaluated based on the extent of methane conversion against time on stream at a CH<sub>4</sub> flow rate of 0.64L/min for 5 hrs run time.

$$\text{Carbon yield (\%)} = \frac{\text{weight of deposited carbon on the catalyst}}{\text{weight of nickel}} \times 100 \quad (3)$$



**Fig. 13** Carbon yield over n-Ni/SiO<sub>2</sub> (0.02) catalyst at respective reaction temperatures.

A huge carbon yield of ~5000% were obtained at 600°C. These observed carbon yield is outstanding compared to many other available results over Ni-based catalyst<sup>55</sup>. The majority of produced nanocarbon is in the form of tubes and very minor quantity can be categorized as very small nanofibers. The main difference between nanotubes and nanofibers is the lack of a hollow cavity for the latter<sup>57</sup>. Many of the nickel particles found located at the tip of the nano carbon. It is apparent from the Fig. 12 (a-c) that the carbon nanotubes are formed with thick walls and the internal cavity are posturing a “fish-bone” or “bamboo” morphology. The varieties of nanocarbon found after decomposition process can be categorized as follows; i) nanocarbons with mouth filled with pear shaped Ni particles (indicated in Fig. 12 with Q symbol), ii) Fish-bone nanocarbon (x), iii) carbon nano tubes with open end (O), iv) carbon nano tubes with closed end (O) and v) carbon nanotube with Ni particle embedded in it (3). The diameter distribution illustrates that more than 90% of nano carbons were appeared with an external diameter of less than 100nm. In addition, it can be speculate that the diameter distribution shifting towards the lower

diameter range as lowering decomposition temperature (Fig. 12 (d-f)). The fraction of carbon nano tubes with diameters above 50nm is higher when decomposition took place at 600°C, while it is comparatively lower at lower temperatures like 550°C and 500°C. Furthermore, previously conducted thorough studies on produced nanocarbon reveals that the outer diameter of the carbon nanotubes greatly depends on the size of Ni particles: larger Ni particle leads to carbon nanotubes with larger diameter<sup>58</sup>. The Ni metal particle found at the tip of the carbon nano tubes are with pear or diamond shape with the sharp tail inserted into the carbon nanotube following tip-growth carbon formation mechanism<sup>59</sup>, which is reinforcing many previous works<sup>60-62</sup>. While, those Ni particle were spherical or sphere shaped embedded in SiO<sub>2</sub> before decomposition process (Fig. 5a). This structural change stipulates the possibility of the existence of Ni particle in the quasi liquid state during the process, even at lower experimental temperature than its melting point (1452°C) and Tamman temperature (726°C). The occurrence of lower temperature quasi liquid is because of formation of highly unstable, compared to Ni and graphite, Ni<sub>3</sub>C metastable compound as an intermediate product in the methane transformation process which can be decomposed to metallic Ni and graphite at lower temperature of 400°C. Furthermore, the higher gradient of Ni<sub>3</sub>C concentration over Ni particle during the process because of the uninterrupted graphite formation sets up a pressure at the graphitic envelope<sup>58</sup>. Hence, mass transfer of carbon occurred by diffusion through the bulk particle as the consequence of built up pressure tries to squeeze out the Ni particle in the quasi liquid state. However, the lower temperature Ni<sub>3</sub>C to metallic Ni and graphite and internal pressure build up explain the change in the shape of Ni particle after TCD process as well as the manifestation of Ni particle inside the carbon nanotubes.

### Extension of method to Fe and Co metals

Co-precipitation cum modified Stöber method to prepare nano-structured catalyst was successfully extended to other metals like Fe and Co with same SiO<sub>2</sub> support. HRTEM images of n-FeO/SiO<sub>2</sub> (0.02)

and n-CoO/SiO<sub>2</sub> (0.02) are shown in Fig. 14. n-FeO and n-CoO were prepared from Iron (III) nitrate nonahydrate ( $\text{Fe}(\text{NO}_3)_3 \cdot 9\text{H}_2\text{O}$ ) and Cobalt (II) Nitrate Hexahydrate ( $\text{Co}(\text{NO}_3)_2 \cdot 6\text{H}_2\text{O}$ ) respectively. Partial agglomeration was observed in both n-FeO/SiO<sub>2</sub> (0.02) and n-CoO/SiO<sub>2</sub> (0.02) because of the magnetic coupling of adjacent metallic phases during silica feeding process. Our results reveal that Co-precipitation cum modified Stöber method can be used as a general method for preparing silica supported metal nano-structures for high temperature requirements.

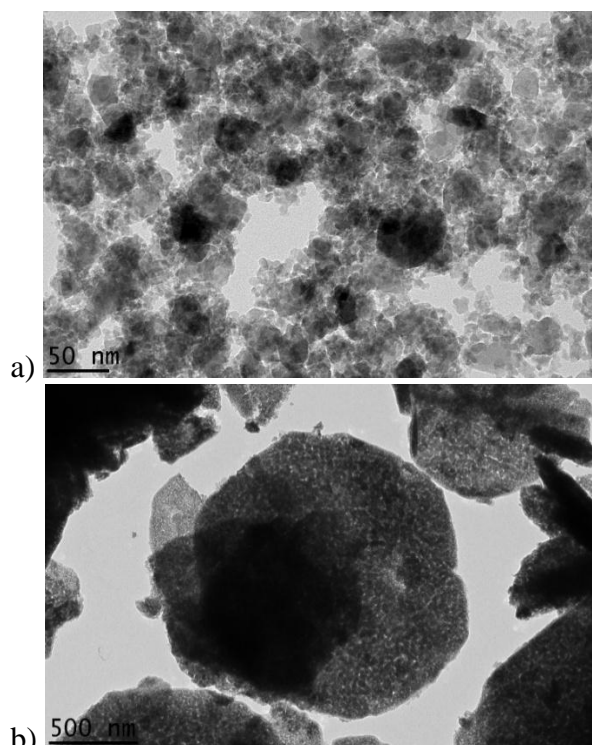


**Fig. 14** HRTEM images of a) n-FeO/SiO<sub>2</sub> (0.02) and b) n-CoO/SiO<sub>2</sub> (0.02).

Preliminary catalytic activity evaluation were conducted over n-Fe/SiO<sub>2</sub> (0.02) and n-Co/SiO<sub>2</sub> (0.02) catalysts. Temperature programmed methane decomposition results are shown in Fig. 15.

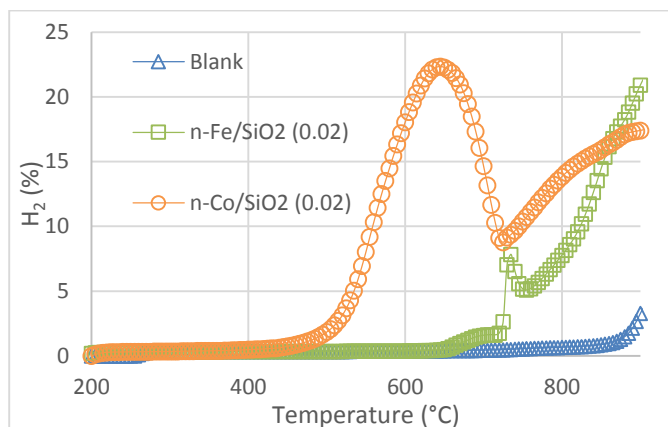


**Fig. 15** Temperature programmed methane decomposition over 1g of n-Fe/SiO<sub>2</sub> (0.02) and n-Co/SiO<sub>2</sub> (0.02) catalysts. Temperature range 200–900°C, flow rate 0.64L/min

Results disclose that n-Fe/SiO<sub>2</sub> (0.02) and n-Co/SiO<sub>2</sub> (0.02) are active for TCD, while not effective as that of n-Ni/SiO<sub>2</sub>. n-Fe/SiO<sub>2</sub> (0.02) is active in the range of 730°C–760°C, while n-Co/SiO<sub>2</sub> (0.02) is active at 500°C to 650°C. Both of them are giving comparatively very less methane conversion than that of n-Ni/SiO<sub>2</sub>. Further isothermal activity studies and mechanism have yet to be conducted. It can be concluded that the activity of studied catalysts are in the following order n-Ni/SiO<sub>2</sub> > n-Co/SiO<sub>2</sub> > n-Fe/SiO<sub>2</sub>.

## Conclusion

n-Ni/SiO<sub>2</sub> catalyst were prepared by co-precipitation cum modified Stöber method and examined for thermocatalytic decomposition of methane. Hydrogen free from GHG was produced over n-Ni/SiO<sub>2</sub> (0.02) catalyst without any significant deactivation at major active temperature range (475°C–600°C) for examined duration of 300 minutes continuously, owing to the fundamental stable nano-structure. Maximum hydrogen production of 40.4% were observed at 600°C, while minimum deactivation after 300 minutes of examination was found at 500°C. Moreover, it was perceived that the higher methane flow rate results a lower methane conversion as well as a higher catalytic deactivation rate. Four different types of carbon nanotubes with inner and outer diameter in tens of nm and length in the range of hundreds of nm were observed after decomposition process. Growth

of nanocarbon found following tip-growth mechanism. Furthermore, the existence of quasi liquid state of Ni-metal explained the encapsulation of metal particles inside the carbon nanotubes as well as the pear/diamond shape of Ni metal after decomposition. Considering the abundance and cheap rate of nickel precursors as well as considerably simple and room temperature catalyst production method, the nano-structured n-Ni/SiO<sub>2</sub> is a kind of promising materials for the production of GHG free H<sub>2</sub> through the catalytic decomposition of methane. The extension of the study for nano-Fe and nano-Co active phases with SiO<sub>2</sub> support reveals that n-Ni/SiO<sub>2</sub> is superior to them in the sense of activity and stability for thermocatalytic decomposition of methane. The activity and stability of examined catalyst are in the following order n-Ni/SiO<sub>2</sub> > n-Co/SiO<sub>2</sub> > n-Fe/SiO<sub>2</sub>. It can be predicted that these type of metal/SiO<sub>2</sub> nanostructures with suitable metals could possibly serve as a catalysts for many high temperature reactions.

## Acknowledgment

The authors gratefully acknowledge financial support from the postgraduate Research Fund (UM.C/HIR/MOHE/ENG/11), University of Malaya, Malaysia.

## Notes and references

\*Corresponding author

Address: Department of Chemical Engineering, University of Malaya, 50603, Kuala Lumpur, Malaysia. Tel.: +60 105023818; Fax: +60 379675319.

E-mail address: [upmashik@gmail.com](mailto:upmashik@gmail.com) (U.P.M. Ashik),

W.M.A. Wan Daud ([ashri@um.edu.my](mailto:ashri@um.edu.my))

† Electronic Supplementary Information (ESI) available: See DOI: 10.1039/b000000x/

1. Y. Li, S. Liu, L. Yao, W. Ji and C.-T. Au, *Catalysis Communications*, 2010, **11**, 368-372.
2. M. Danek, K. F. Jensen, C. B. Murray and M. G. Bawendi, *Chemistry of Materials*, 1996, **8**, 173-180.
3. P. Reiss, J. Bleuse and A. Pron, *Nano Letters*, 2002, **2**, 781-784.
4. M. L. Breen, A. D. Dinsmore, R. H. Pink, S. B. Qadri and B. R. Ratna, *Langmuir*, 2001, **17**, 903-907.
5. V. Skumryev, S. Stoyanov, Y. Zhang, G. Hadjipanayis, D. Givord and J. Nogues, *Nature*, 2003, **423**, 850-853.
6. H. Zeng, J. Li, Z. L. Wang, J. P. Liu and S. Sun, *Nano Letters*, 2003, **4**, 187-190.
7. T. Tsonecheva, L. Ivanova, A. R. Lotz, J. H. Smått, M. Dimitrov, D. Paneva, I. Mitov, M. Linden, C. Minchev and M. Fröba, *Catalysis Communications*, 2007, **8**, 1573-1577.
8. Y. Deng, D. Qi, C. Deng, X. Zhang and D. Zhao, *Journal of the American Chemical Society*, 2007, **130**, 28-29.
9. K. P. Velikov, A. Moroz and A. van Blaaderen, *Applied Physics Letters*, 2002, **80**, 49-51.
10. F. Liu, Y. Qu, Y. Yue, G. Liu and Y. Liu, *RSC Advances*, 2015, **5**, 16837-16846.
11. M. A. Ebiad, D. R. Abd El-Hafiz, R. A. Elsalamony and L. S. Mohamed, *RSC Advances*, 2012, **2**, 8145-8156.
12. R. Z. Sørensen, L. J. E. Nielsen, S. Jensen, O. Hansen, T. Johannessen, U. Quaade and C. H. Christensen, *Catalysis Communications*, 2005, **6**, 229-232.
13. T. Zhang and M. D. Amiridis, *Applied Catalysis A: General*, 1998, **167**, 161-172.
14. R. Aiello, J. E. Fiscus, H.-C. zur Loye and M. D. Amiridis, *Applied Catalysis A: General*, 2000, **192**, 227-234.
15. Y. Li, J. Chen, Y. Qin and L. Chang, *Energy & Fuels*, 2000, **14**, 1188-1194.
16. J. W. Gosselink, *International Journal of Hydrogen Energy*, 2002, **27**, 1125-1129.
17. U. P. M. Ashik, W. M. A. Wan Daud and H. F. Abbas, *Renewable and Sustainable Energy Reviews*, 2015, **44**, 221-256.
18. M. Balat and M. Balat, *International Journal of Hydrogen Energy*, 2009, **34**, 3589-3603.
19. L. B. Brentner, J. Peccia and J. B. Zimmerman, *Environmental Science & Technology*, 2010, **44**, 2243-2254.
20. H. F. Abbas and W. M. A. W. Daud, *Applied Catalysis A: General*, 2010, **388**, 232-239.
21. S. Wang, *Environmental Science & Technology*, 2008, **42**, 7055-7063.
22. V. M. Shinde and G. Madras, *RSC Advances*, 2014, **4**, 4817-4826.
23. R. A. Elsalamony, D. R. Abd El-Hafiz, M. A. Ebiad, A. M. Mansour and L. S. Mohamed, *RSC Advances*, 2013, **3**, 23791-23800.
24. P. Westermann, B. Jørgensen, L. Lange, B. K. Ahring and C. H. Christensen, *International Journal of Hydrogen Energy*, 2007, **32**, 4135-4141.

25. M. N. Uddin, W. M. A. W. Daud and H. F. Abbas, *RSC Advances*, 2014, **4**, 10467-10490.
26. P. Jana, V. A. de la Peña O'Shea, J. M. Coronado and D. P. Serrano, *International Journal of Hydrogen Energy*, 2012, **37**, 7034-7041.
27. K. Otsuka, S. Kobayashi and S. Takenaka, *Journal of Catalysis*, 2001, **200**, 4-9.
28. T. V. Choudhary, C. Sivadinarayana, C. C. Chusuei, A. Klinghoffer and D. W. Goodman, *Journal of Catalysis*, 2001, **199**, 9-18.
29. K. Otsuka, S. Kobayashi and S. Takenaka, *Applied Catalysis A: General*, 2000, **190**, 261-268.
30. S. Takenaka, H. Ogihara, I. Yamanaka and K. Otsuka, *Applied Catalysis A: General*, 2001, **217**, 101-110.
31. L. Li, S. He, Y. Song, J. Zhao, W. Ji and C.-T. Au, *Journal of Catalysis*, 2012, **288**, 54-64.
32. W. Stöber, A. Fink and E. Bohn, *Journal of Colloid and Interface Science*, 1968, **26**, 62-69.
33. A. A. Al-Hassani, H. F. Abbas and W. M. A. Wan Daud, *International Journal of Hydrogen Energy*, 2014, **39**, 7004-7014.
34. M. Stjerndahl, M. Andersson, H. E. Hall, D. M. Pajerowski, M. W. Meisel and R. S. Duran, *Langmuir*, 2008, **24**, 3532-3536.
35. J. Zou, Y.-G. Peng and Y.-Y. Tang, *RSC Advances*, 2014, **4**, 9693-9700.
36. J. C. Park, J. U. Bang, J. Lee, C. H. Ko and H. Song, *Journal of Materials Chemistry*, 2010, **20**, 1239-1246.
37. Y. Li, J. Chen, L. Chang and Y. Qin, *Journal of Catalysis*, 1998, **178**, 76-83.
38. L. Yao, T. Shi, Y. Li, J. Zhao, W. Ji and C.-T. Au, *Catalysis Today*, 2011, **164**, 112-118.
39. S. D. Robertson, B. D. McNicol, J. H. De Baas, S. C. Kloet and J. W. Jenkins, *Journal of Catalysis*, 1975, **37**, 424-431.
40. L. Li, P. Lu, Y. Yao and W. Ji, *Catalysis Communications*, 2012, **26**, 72-77.
41. X.-K. Li, W.-J. Ji, J. Zhao, S.-J. Wang and C.-T. Au, *Journal of Catalysis*, 2005, **236**, 181-189.
42. R. Xie, D. Li, B. Hou, J. Wang, L. Jia and Y. Sun, *Catalysis Communications*, 2011, **12**, 380-383.
43. A. Romero, A. Garrido, A. Nieto-Márquez, P. Sánchez, A. d. Lucas and J. L. Valverde, *Microporous and Mesoporous Materials*, 2008, **110**, 318-329.
44. S. Takenaka, S. Kobayashi, H. Ogihara and K. Otsuka, *Journal of Catalysis*, 2003, **217**, 79-87.
45. S. H. Joo, J. Y. Park, C.-K. Tsung, Y. Yamada, P. Yang and G. A. Somorjai, *Nat Mater*, 2009, **8**, 126-131.
46. J. Wu, F. Hu, X. Hu, Z. Wei and P. K. Shen, *Electrochimica Acta*, 2008, **53**, 8341-8345.
47. W.-M. Zhang, J.-S. Hu, Y.-G. Guo, S.-F. Zheng, L.-S. Zhong, W.-G. Song and L.-J. Wan, *Advanced Materials*, 2008, **20**, 1160-1165.
48. W. Wang, H. Wang, Y. Yang and S. Jiang, *International Journal of Hydrogen Energy*, 2012, **37**, 9058-9066.
49. B. Zapata, M. A. Valenzuela, J. Palacios and E. Torres-Garcia, *International Journal of Hydrogen Energy*, 2010, **35**, 12091-12097.
50. G. D. B. Nuernberg, E. L. Foletto, C. E. M. Campos, H. V. Fajardo, N. L. V. Carreño and L. F. D. Probst, *Journal of Power Sources*, 2012, **208**, 409-414.
51. J. L. Figueiredo, J. J. M. Órfão and A. F. Cunha, *International Journal of Hydrogen Energy*, 2010, **35**, 9795-9800.
52. A. F. Cunha, J. J. M. Órfão and J. L. Figueiredo, *Applied Catalysis A: General*, 2008, **348**, 103-112.
53. M. Nasir Uddin, W. M. A. Wan Daud and H. F. Abbas, *Energy Conversion and Management*, 2015, **90**, 218-229.
54. M. S. Kim, N. M. Rodriguez and R. T. K. Baker, *Journal of Catalysis*, 1991, **131**, 60-73.
55. S. K. Saraswat and K. K. Pant, *International Journal of Hydrogen Energy*, 2011, **36**, 13352-13360.
56. S.-P. Chai, C.-M. Seah and A. R. Mohamed, *Journal of Natural Gas Chemistry*, 2011, **20**, 84-89.
57. P. Serp, M. Corrias and P. Kalck, *Applied Catalysis A: General*, 2003, **253**, 337-358.
58. J. C. Guevara, J. A. Wang, L. F. Chen, M. A. Valenzuela, P. Salas, A. García-Ruiz, J. A. Toledo, M. A. Cortes-Jácome, C. Angeles-Chavez and O. Novaro, *International Journal of Hydrogen Energy*, 2010, **35**, 3509-3521.
59. A. K. Sinha, D. W. Hwang and L.-P. Hwang, *Chemical Physics Letters*, 2000, **332**, 455-460.
60. T. Baird, J. R. Fryer and B. Grant, *Carbon*, 1974, **12**, 591-602.
61. R. T. K. Baker, M. A. Barber, P. S. Harris, F. S. Feates and R. J. Waite, *Journal of Catalysis*, 1972, **26**, 51-62.
62. P. A. Tesner, E. Y. Robinovich, I. S. Rafalkes and E. F. Arefieva, *Carbon*, 1970, **8**, 435-442.